



Article

Ti_nO_{2n-1} Suboxide Phases in TiO₂/C Nanocomposites Engineered by Non-hydrolytic Sol–Gel with Enhanced Electrocatalytic Properties

Shuxian Zou, Romain Berthelot , Bruno Boury , Pierre Hubert Mutin and Nicolas Brun *

ICGM, Univ Montpellier, CNRS, ENSCM, Montpellier, France; shuxian.zou@etu.unistra.fr (S.Z.);

romain.berthelot@umontpellier.fr (R.B.); bruno.boury@umontpellier.fr (B.B.);

hubert.mutin@umontpellier.fr (P.H.M.)

* Correspondence: nicolas.brun@enscm.fr

Received: 28 July 2020; Accepted: 3 September 2020; Published: 9 September 2020



Abstract: We report a non-hydrolytic sol-gel (NHSG) route to engineer original mesoporous Ti_nO_{2n-1}@TiO₂/C nanocomposites. The synthetic approach is straightforward, solvent-free, additive-free, and meets the challenge of atom economy, as it merely involves TiCl₄ and THF in stoichiometric amounts. We found that these nanocomposites present enhanced electrocatalytic properties towards the oxygen reduction reaction (ORR) in 0.1 M KOH. We believe that these preliminary results will open a window of opportunity for the design of metal suboxides/carbon nanocomposites through NHSG routes.

Keywords: nanocomposite; nanocrystal; nanostructure; non-hydrolytic sol-gel; atom-economic synthesis; carbothermal reduction; titanium suboxide; magnéli phases; electrocatalysis; ORR

1. Introduction

Titanium suboxides have received considerable attention in the last decades due to their remarkable electronic and optical properties [1–3]. Titanium suboxides can be classified in two main families [4,5]: (i) oxygen-deficient titanium oxides, namely, TiO_{2-x} (where 0.001 > x > 0) or black TiO₂ [6], which present point defects such as oxygen vacancies and titanium interstitials [7]; (ii) Magnéli phases, namely, TiO_{2-x} (where 0.25 > x > 0.001), for which the off-stoichiometry is accommodated by extended defects and changes in the crystal structure. Magnéli phases, also noted as Ti_nO_{2n-1} (where n varies from 4 to 37) and first described in the 1950s by Magnéli et al. [8,9], present crystallographic shear (CS) planes, and can be seen as ordered combinations of rutile TiO₂ and corundum Ti₂O₃ structures [3,4]. Note that, in contrast to Magnéli phases, Ti₃O₅ structures [10] (Ti_nO_{2n-1}, where n = 3) have no CS planes. However, as they satisfy the Ti_nO_{2n-1} formula, Ti₃O₅ polymorphs have often been considered as the first members of the Magnéli phases' family. Titanium suboxides depict remarkable properties [3,11,12], amongst which are electrochemical stability, high electronic conductivity (c.a. 10.4 S cm⁻¹ for Ti₄O₇ at room temperature [13]), high electron mobility (>0.5 cm² V⁻¹ s⁻¹ for Ti₄O₇ at room temperature [1]), and low band-gap as compared with stoichiometric TiO₂ (about 0.5 eV smaller than that of TiO₂ anatase [14]). Thus, titanium suboxides have been widely investigated in electrocatalysis [15–19], photocatalysis [20–23] and energy storage devices [24,25].

Several synthesis routes have been reported in the literature for the preparation of titanium suboxides, either defective or Magnéli phases. Most of them start from stoichiometric TiO₂ and involve oxygen scavengers such as zirconium foil [19,26] and/or reducing agents such as carbon (through carbothermal reduction) [27–29], CaH₂ at low temperature (350–450 °C) [30,31], or hydrogen gas at temperatures typically higher than 950 °C [24]. Amongst them, the carbothermal reduction

approach is particularly interesting. It generally implies external carbon sources, usually from organic additives, combined to the oxide by sol-gel process and yielding, after carbothermal reduction, Ti_nO_{2n-1}/C composites in simple, one-pot, bottom-up approaches [28]. The sol-gel process has been largely used for the preparation of advanced metal-oxide materials, such as TiO_2 . This process presents numerous advantages, including versatility and scalability, and can be conducted under mild condition ($T \leq 100$ °C, 1 atm). Regarding titanium suboxides, a few studies have been reported on sol-gel/carbothermal reduction routes starting from commercial titanium alkoxides and organic additives, such as poly(ethyleneimine), polyethyleneglycol [28], poly(styrene-*b*-2-vinylpyridine) [32], resol [25], or glucose [29]. Following such a procedure, Portehault et al. [28] obtained single-phase Magnéli/carbon nanocomposites with both structural (Ti_nO_{2n-1} with $n = 8, 6, 5, 4,$ or 3) and textural control by tuning the Ti:C ratio, the nature of the carbon source and the calcination atmosphere (argon versus nitrogen). More recently, Huang et al. [29] prepared various Ti_nO_{2n-1}/C nanocomposites employing glucose as the carbon source and a carbothermal reduction process under vacuum. The authors demonstrated the importance of the cooling conditions which govern the predominant titanium suboxide phase obtained in fine ($n = 4, 3, 2,$ or 1). Those are two good examples that demonstrate the versatility of the sol-gel process combined to carbothermal reduction to design Ti_nO_{2n-1}/C nanocomposites. Although innovative and efficient, most of these approaches rely on relatively expensive precursors (e.g., synthetic polymers) and/or require organic additives in a large excess, making the all procedure wasteful of resources. With this aim, we propose hereafter to investigate an original one-pot, atom-economic synthesis route to prepare Ti_nO_{2n-1}/C nanocomposites using the non-hydrolytic sol-gel process (NHSG).

Unlike conventional aqueous sol-gel processes, NHSG is performed in organic medium and involves organic oxygen donors such as ethers or alcohols instead of water [33,34]. NHSG offers simple, one-step routes to produce oxide-based materials with well controlled compositions and textures, avoiding the use of expensive precursors or reactivity modifiers [33]. The main drawback of NHSG lies in the necessity to work under anhydrous conditions and at higher temperature (up to 200 °C) and pressure (up to c.a. 30 bars) than conventional aqueous sol-gel methods, which may hamper industrial applications. Nevertheless, NHSG has been established as a versatile methodology for the synthesis of mesoporous metal-oxides and mixed oxides in the absence of templating agents or costly drying procedures [35], metal oxide nanocrystals [36–39] as well as organic-inorganic hybrids [40,41] and metal-oxide/carbon nanocomposites [42,43]. Recently, we reported a solvent-free NHSG route to synthesize TiO_2/C nanocomposites based on the reaction of simple ethers (diisopropyl ether or tetrahydrofuran, THF) in a stoichiometric amount with titanium tetrachloride [42]. In this atom-economic process, the ether acted not only as an oxygen donor, but also as the sole carbon source, yielding anatase TiO_2 nanocrystals coated by an amorphous carbon film [42]. Herein, we further extend this original approach to the preparation of titanium suboxides, by demonstrating that Ti_nO_{2n-1} phases can be easily generated by partial carbothermal reduction of the TiO_2/C nanocomposites at relatively low temperature, i.e., 950 °C, under argon flow. This solvent-free, additive-free approach is straightforward, and the partial reduction of TiO_2 into Ti_nO_{2n-1} phases (with $2 \leq n \leq 6$) allows engineering original mesoporous $Ti_nO_{2n-1}@TiO_2/C$ nanocomposites. The latter are rarely targeted as such, researchers generally focussing on pure phases, but we found that this nano-assembly presents enhanced electrocatalytic properties towards the oxygen reduction reaction (ORR) in 0.1 M KOH. We believe that these preliminary results open new opportunities for the atom-economic design of metal suboxides/carbon nanocomposites through NHSG routes.

2. Materials and Methods

2.1. Materials Synthesis

To avoid water, all manipulations were carried out in a glovebox under argon atmosphere (<10 ppm of water and O_2). Titanium(IV) chloride 99%, (Sigma-Aldrich Chemie, Saint-Quentin

Fallavier, France) was used as received. Tetrahydrofuran (THF) 99.8%, (Fisher Scientific, Hampton, NH, USA) was dried over a PureSolve MD5 solvent purification system (Innovative Technology Inc., Amesbury, MA, USA). The amount of water in THF was controlled with a Karl Fischer coulometer (SI Analytics, Mainz, Germany) before reaction ($H_2O < 5$ ppm).

The synthesis route is well-established and was already reported in our previous work [42]. Typically, $TiCl_4$ (12.52 mmol, 1.37 mL) and THF (25.04 mmol, 2.03 mL) were added into a 23 mL stainless steel digestion vessel with a polytetrafluoroethylene (PTFE) lining from Parr Instrument Company (Moline, IL, USA). The sealed digestion vessel was heated in an oven at 180 °C for 4 days under autogenous pressure. The gel was dried under vacuum at 120 °C for 5 h, yielding a xerogel labeled xer- TiO_2 . The resulting xerogel was pyrolyzed under argon atmosphere (50 mL min^{-1}) at 850 or 950 °C for 1 to 8 h (heating rate 10 °C min^{-1}) to obtain $Ti_nO_{2n-1}@TiO_2/C$ nanocomposites. These nanocomposites are labeled $TiO_2/C-x-y$, with x the first digit of the plateau temperature in degrees Celsius; and y the duration at the plateau in hours. For example, $TiO_2/C-9-8$ stands for the sample pyrolyzed at 950 °C for 8 h. For comparison, a TiO_2 sample was obtained by calcination in air (50 mL min^{-1}) of the xerogels at 500 °C for 5 h (heating rate 10 °C min^{-1}). This sample is labeled TiO_2-5-5 .

2.2. Characterization

Thermogravimetric analyses (TGA) were carried out using a Netzsch Simultaneous Thermal Analyzer STA 409 PC Luxx (Netzsch, Selb, Germany), with a heating rate of 10 °C min^{-1} in the 20–1000 °C range, under a dry air atmosphere or under argon (50 mL min^{-1}). X-Ray diffraction (XRD) patterns were obtained using a PANalytical X'Pert Pro MPD diffractometer (Malvern PANalytical Ltd, Malvern, UK), with the $K\alpha$ radiation of Cu ($\lambda = 1.5418$ Å) and a step size of 0.033° (2 θ scale) into the 10–70° interval. N_2 -physisorption experiments were carried out at –196 °C on a Micromeritics TriStar 3000 (Micromeritics France, Merignac, France). Samples were out-gassed under vacuum at 110 °C overnight. Equivalent BET specific surface areas (SSA_{BET}) were determined in the relative pressure range P/P_0 from 0.08 to 0.25. The total pore volume ($V_{0.99}$) was measured at $P/P_0 = 0.99$. Transmission electron microscopy (TEM) images were acquired with a JEOL 1200 microscope (JEOL Europe, Croissy sur Seine, France). High resolution TEM analysis was performed on a JEOL 2200FS microscope (JEOL Europe, Croissy sur Seine, France) operated at 200 kV from the MEA platform (Université de Montpellier, Montpellier, France). This microscope is equipped with a field emission gun (FEG) and an in-column Omega-type energy filter. STEM-EDX (Scanning Transmission Electron Microscopy) mapping were performed using a probe size of 1.5 nm and X-rays measured with a silicon drift detector (30 mm², JEOL) with a collection solid angle of 0.13 sr.

2.3. Electrochemical Properties

A standard ink was prepared by mixing 10 mg of material with 300 μ L of a Nafion[®] binder solution and 700 μ L of absolute ethanol. The ink was ultrasonicated for at least 30 min for homogenization. A 5 μ L aliquot was dropped onto a freshly polished glassy carbon rotating disk electrode (diameter 3 mm, electrode area 0.071 cm²) to prepare a catalyst thin film. The electrode was warmed to 40 °C in an oven prior to ink application in order to achieve better electrode coverage of the catalyst film. Electrochemical tests were performed in 0.1 M KOH (70 mL) in a standard three-electrode setup with an Ag/AgCl reference electrode and a Pt wire counter electrode. We used a RRDE-3A device (ALS Co. Ltd, Tokyo, Japan) to perform the rotating disk electrode (RDE) hydrodynamic measurements, a BioLogic VSP-300 potentiostat (BioLogic, Seyssinet-Pariset, France) and the EC-Lab[®] Software (BioLogic, Seyssinet-Pariset, France). Koutecky–Levich analyses were performed as described in literature [44] (for more details, see Appendix A).

3. Results

3.1. Synthesis and Characterization

3.1.1. NHSG Ether Route and Carbothermal Reduction: Mechanistic Insights

The NHSG ether route has been extensively used to prepare metal oxides, especially for the synthesis of titanium oxides [33,35,45]. In our previous works, we reported on the synthesis of TiO₂ nanocrystals and TiO₂/C nanocomposites from TiCl₄ and THF [42]. This approach is based on the intermediate formation of alkoxide groups, which then condense with Ti-Cl to form oxo bridges (step (1) in Figure 1). In the case of THF and at moderate temperature (below 110 °C), the major organic by-product is 1,4-dichlorobutane. At higher reaction temperature, typically at 180 °C as used herein, secondary reactions are favoured, especially the formation and polymerization of alkenes resulting from the elimination of HCl (step (2) and (3) in Figure 1). These reactions, most probably catalyzed by the freshly produced TiO₂ particles and HCl, can form highly cross-linked polymers, as shown in Figure 1. In a previous article [42], we showed that after pyrolysis at 750 °C under argon, we could take advantage of these highly cross-linked polymers to prepare TiO₂/C nanocomposites (step (4) in Figure 1). Herein, we propose to investigate thermal post-treatments at higher temperatures, i.e., 850 and 950 °C, and to explore the opportunity to design Ti_nO_{2n-1}@TiO₂/C nanocomposites through carbothermal reduction (step (5) in Figure 1).

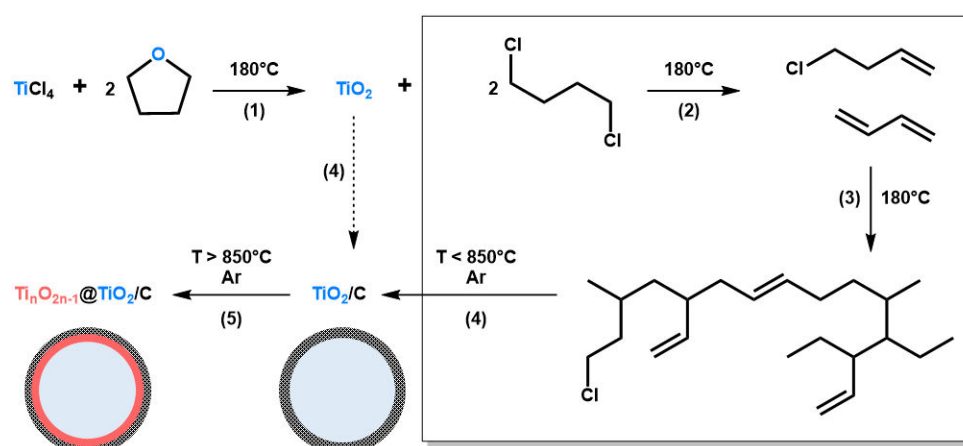


Figure 1. Schematic representation of the non-hydrolytic sol-gel (NHSG) route developed herein to prepare TiO₂, TiO₂/C and Ti_nO_{2n-1}@TiO₂/C nanocomposites. (1) Alkoxylation/Condensation; (2) Dehydrochlorination; (3) Polymerization; (4) Carbonization; and (5) Partial carbothermal reduction. In this representation, xer-TiO₂ corresponds to TiO₂ together with organic by-products (box on the right side) before step (4).

The presence of a large amount of organic cross-linked polymers in the xerogel obtained right after NHSG and subsequent drying, labeled xer-TiO₂, was confirmed by thermogravimetric analysis (TGA) under synthetic dry air flow, as shown by the weight loss of about 31 wt.% from 240 °C to 550 °C (Figure 2a). To assess the carbothermal reduction process, TGA was also performed under argon flow on xer-TiO₂ (Figure 2b). As mentioned above, this xerogel contains TiO₂, oxygen-poor cross-linked polymers, and some residual chlorine atoms bonded to carbon [42]. On the TGA curve, three main weight loss regions can be seen: (i) in the temperature range 40–200 °C, with a weight loss of about 2 wt.%; (ii) in the temperature range 280–500 °C, with a weight loss of about 14 wt.%; and (iii) in the temperature range 850–1000 °C, with a weight loss of about 2 wt.% (Figure 2b). While the first region is most probably related to the elimination of residual volatile compounds, the second region can be attributed to the carbonization of the cross-linked polymers through inter- and intramolecular reactions such as dehydrochlorination. The third region might be attributed to the partial carbothermal reduction of TiO₂ to Ti_nO_{2n-1}.

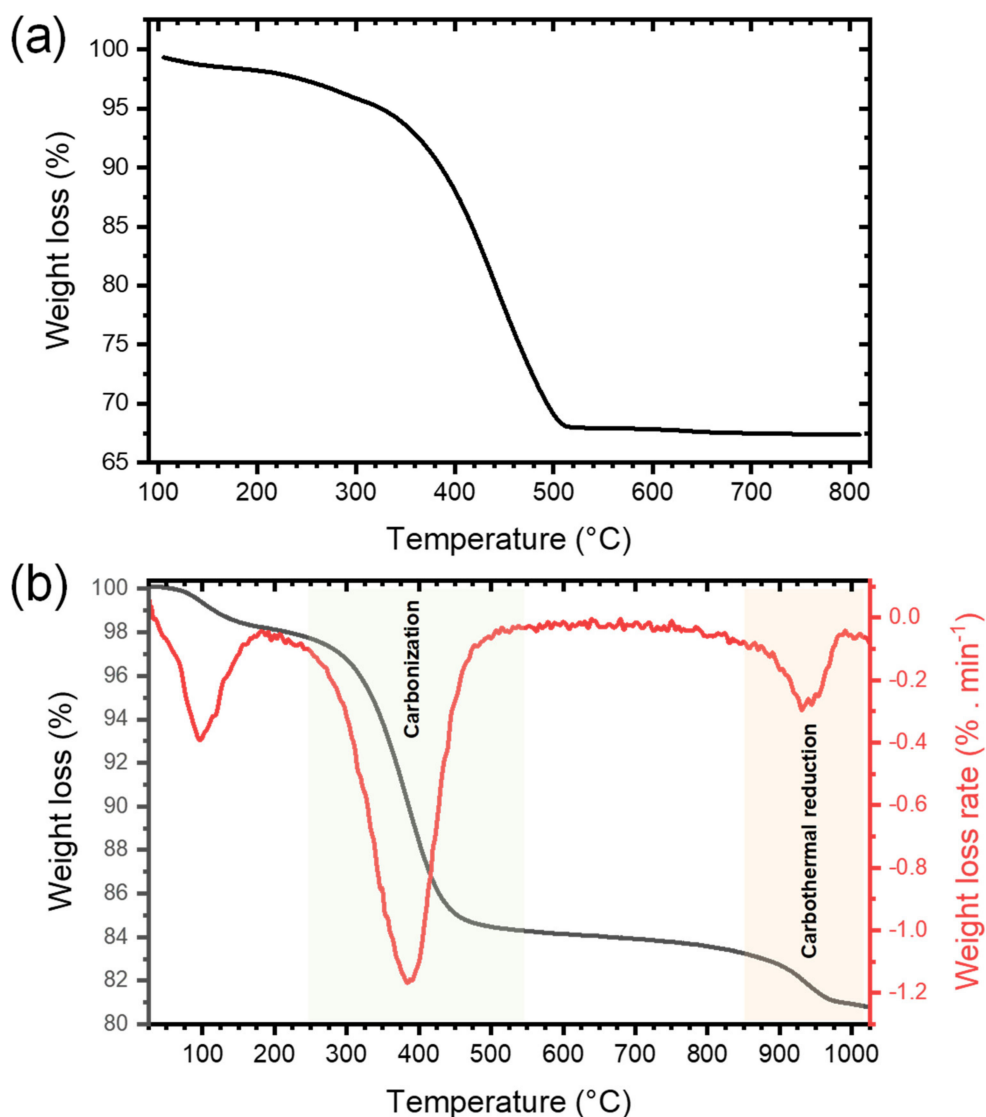


Figure 2. Thermogravimetric analyses performed (a) under synthetic dry air flow (50 mL min^{-1}) and (b) under argon flow (50 mL min^{-1}) at $10^\circ\text{C min}^{-1}$ of xer-TiO₂.

3.1.2. TiO₂ and TiO₂/C Nanocomposites: Characterization

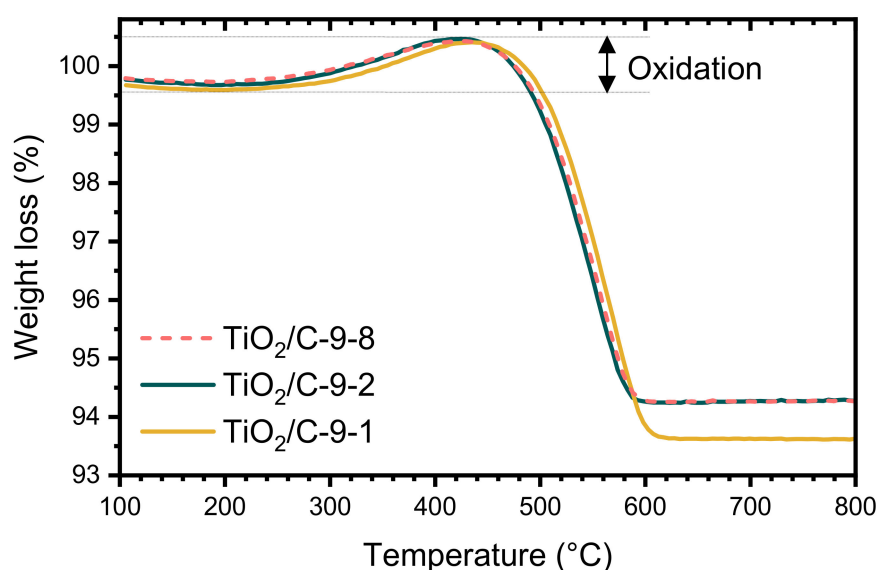
TiO₂/C nanocomposites were prepared by pyrolysis of xer-TiO₂ at 950°C for 1, 2 and 8 h. For comparison, xer-TiO₂ was also pyrolyzed at 850°C for 4 h, or calcined in air at 500°C for 5 h. These materials were thoroughly characterized by TGA, elemental analysis, X-ray diffraction (XRD), nitrogen sorption at 77 K, and transmission electron microscopy (TEM).

The TGA curves of the samples pyrolyzed at 950°C (TiO₂/C-9-*y* samples) were nearly identical, whatever the duration of the pyrolytic treatment. The total weight loss is much lower than the one of xer-TiO₂ (c.a. 6–7 wt.%, Table 1) and starts at higher temperature, above 450°C . Interestingly, a significant weight gain was observed in the temperature range $300\text{--}500^\circ\text{C}$ for the TiO₂/C-9-*y* samples (Figure 3). This feature can be ascribed to the re-oxidation of titanium suboxides and has already been reported for Ti_{*n*}O_{2*n*-1}/C nanocomposites in the same temperature range [29].

Table 1. Chemical composition, textural and structural properties of xer-TiO₂, TiO₂-5-5 and the different TiO₂/C-*x-y* samples.

Sample	Organic (wt%) [†]	C (wt%) [‡]	H (wt%) [‡]	SSA _{BET} (m ² g ⁻¹) [#]	V _{0.99} (cm ³ g ⁻¹)	TiO ₂ Phase(s)	Ti _n O _{2n-1} Phases
xer-TiO ₂	31 ± 3	20 ± 2	2.4 ± 0.2	4	0.02	Anatase (A)	None
TiO ₂ -5-5	n/a	n/a	n/a	60	0.16	A	None
TiO ₂ /C-8-4	4.0 ± 0.4	5.0 ± 0.1	0.1	79	0.23	A/Rutile (R)	None
TiO ₂ /C-9-1	6.8 ± 0.6	6.3 ± 0.1	< 0.1	150	0.35	A	Ti ₃ O ₅ /Ti ₆ O ₁₁
TiO ₂ /C-9-2	6.2 ± 0.5	n/a	n/a	130	0.31	A	Ti ₃ O ₅ /Ti ₆ O ₁₁
TiO ₂ /C-9-8	6.2 ± 0.5	6.3 ± 0.1	< 0.1	124	0.30	A	Ti ₃ O ₅ /Ti ₆ O ₁₁

[†] TGA weight loss from 150 to 800 °C; [‡] Elemental analysis; [#] BET equivalent specific surface area; Total pore volume determined at P/P₀ = 0.99.

**Figure 3.** Thermogravimetric analyses (TGA) performed under synthetic dry air flow (50 mL min⁻¹) at 10 °C min⁻¹ of TiO₂/C-9-*y* samples.

The formation of titanium suboxide in the TiO₂/C-*x-y* samples was confirmed by XRD (Figure 4, Table 1). While anatase (A) was the major phase present in all the samples, several peaks attributed to Ti₃O₅ (monoclinic) and Ti₆O₁₁ were observed for the TiO₂/C-9-*y* samples, showing that carbothermal reduction of TiO₂ occurred at 950 °C. Conversely, in the case of the sample pyrolyzed at 850 °C, TiO₂/C-8-4, a significant amount of rutile (R) was detected, as reported in our previous work [42], but no suboxide phase was identified, indicating that carbothermal reduction did not take place at this temperature. The presence of a substantial amount of anatase (A) after pyrolysis at 850 °C and 950 °C is remarkable, since the anatase to rutile crystal transition usually occurs below 700 °C [46]. As reported in literature [47], the presence of carbon layers onto coated titanium dioxide particles can suppress the anatase to rutile phase transformation by preventing sintering and crystal growth. In our previous works [42,48], the same feature was observed for TiO₂/C nanocomposites prepared by a similar NHSG procedure and pyrolyzed under argon atmosphere at 750 and 900 °C. Our results suggested that the carbon content, which was related to the thickness of the carbon layer onto TiO₂ nanoparticles, strongly affects the anatase to rutile crystal transition [48]. No significant difference was observed between the patterns of the three samples of the TiO₂/C-9-*y* series, confirming that the duration of the pyrolytic treatment did not influence the carbothermal reduction process. Note that the sole difference, observed in the 32–33° (2θ) region (Figure 4), suggests that a longer pyrolytic treatment at 950 °C might favor Ti₆O₁₁ over Ti₃O₅. Even though elemental analysis and TGA indicated that about 6 wt.% C remained in the TiO₂/C-9-*y* samples, the presence of anatase indicates that the

carbothermal reduction at 950 °C was incomplete, whereas in recent studies reported in the literature, either single-phase Magnéli [28,32] or predominant suboxide phases with a small amount of rutile and anatase [29] were obtained by carbothermal reduction below 1000 °C. Particularly, Huang et al. [29] obtained various titanium suboxides from Ti_4O_7 to TiO with a C:Ti molar ratio in the xerogel between 1.1 and 6.5. In our case, we employed a C:Ti molar ratio of 1.9 (i.e., 20 wt.% of carbon in xer- TiO_2 , Table 1), which should theoretically be sufficient to fully reduce TiO_2 . While the C:Ti molar ratio did not seem critical herein, several factors may explain the incomplete reduction of TiO_2 . This will be discussed later.

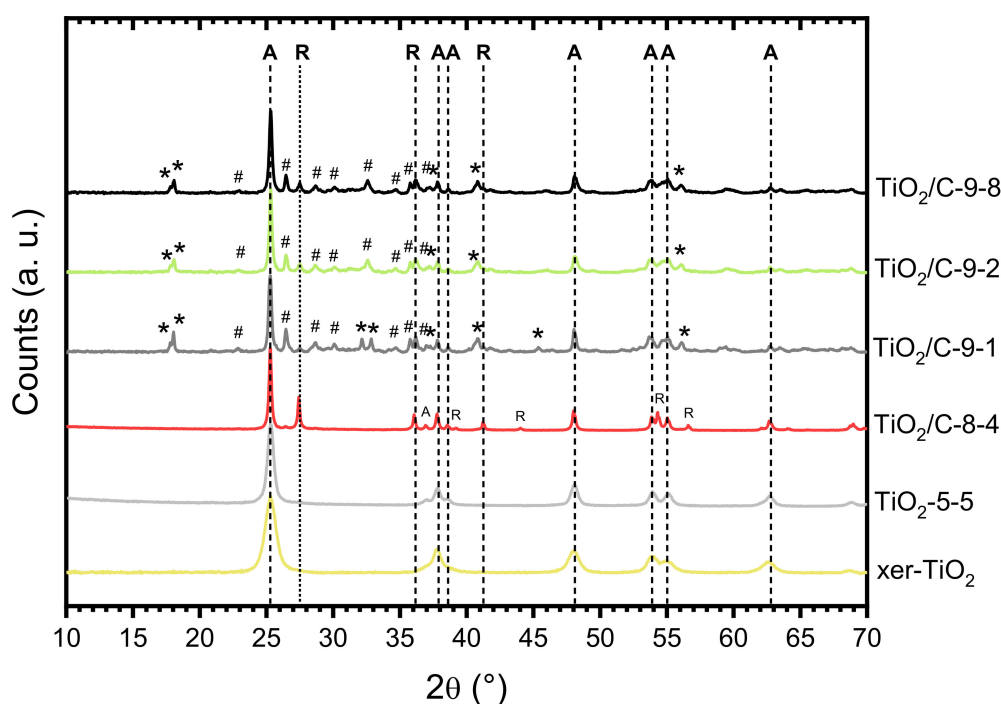


Figure 4. X-ray diffraction (XRD) patterns of xer- TiO_2 , TiO_2 -5-5, and the TiO_2/C - x - y series. A: Anatase; R: Rutile; *: Ti_3O_5 (monoclinic); #: Ti_6O_{11} .

Besides structural properties, textural and morphological properties were investigated. The nitrogen sorption isotherms of xer- TiO_2 , TiO_2 -5-5, and the TiO_2/C - x - y series are shown in Figure 5. The associated textural data are compiled in Table 1. All the samples are mesoporous, which is in good agreement with our previous works on TiO_2 -based materials obtained by NHSG ether routes [42]. According to the IUPAC classification [49], the isotherms are of type IV, corresponding to mesoporous solids with interparticle porosity. The TiO_2/C - x - y samples, especially the ones treated at 950 °C, depict significantly higher specific surface areas and pore volumes than xer- TiO_2 and TiO_2 -5-5. This feature suggests that the carbonaceous phase is highly porous, most probably due to the thermal degradation of the organic cross-linked polymer phase during pyrolysis.

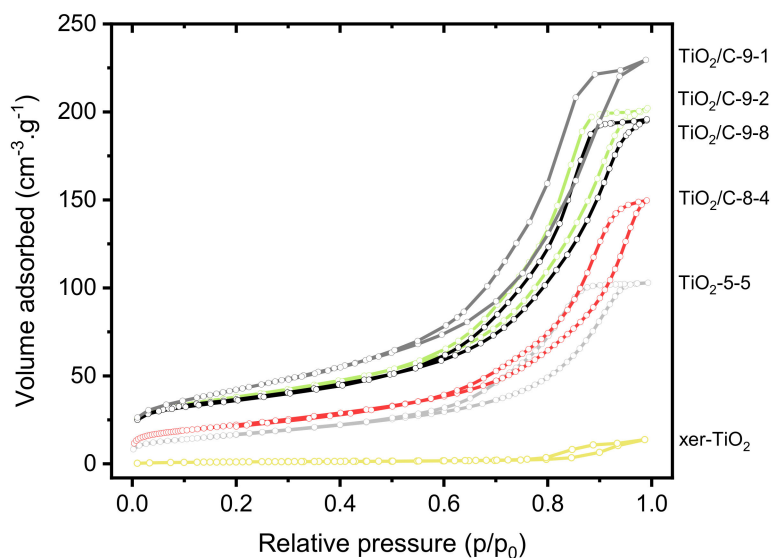


Figure 5. Nitrogen sorption isotherms at 77 K of xer-TiO₂, TiO₂-5-5 and the different TiO₂/C-*x-y* samples prepared herein.

The presence of a porous carbon phase was confirmed by TEM (Figure 6). While xer-TiO₂ is composed of large agglomerates of TiO₂ anatase nanocrystals with a diameter inferior to 20 nm (Figure 6a), TiO₂/C-9-1 is composed of larger nanoparticles of ca. 50 nm embedded in a mesoporous carbon matrix (Figure 6b,c). These mesopores have a diameter of ca. 10 nm, in the range of the native TiO₂ anatase nanocrystals. One may assume that these mesopores were generated during the thermal post-treatment, due to the migration/growth of TiO₂ nanocrystals through the carbon matrix and the consumption of carbon atoms during the carbothermal reduction process. STEM-EDX mapping on TiO₂/C-9-1 confirmed that TiO₂ and/or Ti_{*n*}O_{2*n*-1}@TiO₂ nanocrystals are surrounded by a carbon film.

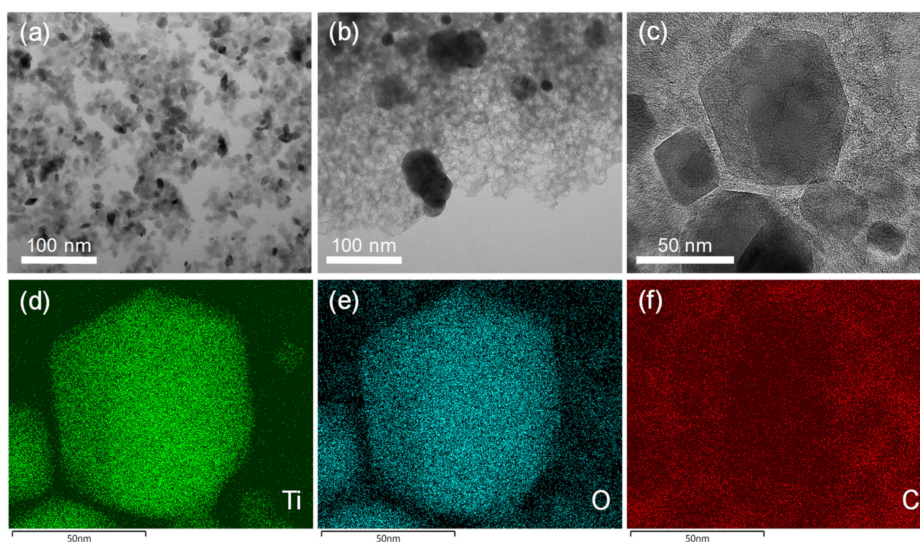
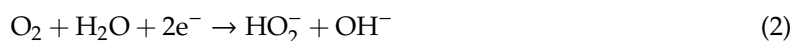


Figure 6. Transmission electron microscopy (TEM) images of (a) xer-TiO₂ and (b) TiO₂/C-9-1. (c) High resolution TEM image and (d–f) STEM-EDX mapping of TiO₂/C-9-1. The corresponding element (Ti, O or C) is noted in the bottom left corner of each image.

3.2. Electrochemical Properties Towards the Oxygen Reduction Reaction (ORR)

To demonstrate the superior properties of the Ti_{*n*}O_{2*n*-1}@TiO₂/C nanocomposites prepared herein, we proposed to assess their electrocatalytic activity towards the oxygen reduction reaction (ORR). The ORR is one of the most studied reactions in the field of electrochemistry, especially when dealing

with energy storage and conversion devices [50,51]. In particular, ORR in aqueous alkaline media [52] has been widely studied and is of great interest for applications in metal-air batteries [53] and alkaline anion-exchange membrane fuel cells [54]. In aqueous alkaline media, ORR can proceed either by a direct four-electron pathway to directly reduce O₂ into hydroxide ions (Equation (1)), or by a two-electron pathway with formation of peroxide ions as intermediate species (Equation (2)), followed by a two-electron reduction to hydroxide ions (Equation (3)) or disproportionation (Equation (4)).



Cyclic voltammetry (CV) measurements were carried out in O₂-saturated 0.1 M KOH solution. The CV curves obtained for TiO₂/C-9-1 present a well-defined cathodic peak centered between −0.3 and −0.4 V vs. Ag/AgCl (Figure 7a), demonstrating the electrocatalytic activity of this material towards the ORR. In order to thoroughly compare the electrochemical properties of each material, linear sweep voltammetry (LSV) was performed and polarization curves were recorded from 0.2 to −1.0 V vs. Ag/AgCl, at a rotation rate of 1600 rpm (Figure 7b). The presence of an intermediary current plateau (between −0.4 and −0.6 V for TiO₂/C-9-*y*; and between −0.5 and −0.7 V for TiO₂/C-8-4, TiO₂-5-5 and xer-TiO₂) can be attributed to several factors, and may suggest either: (i) a mass transport limitation (e.g., difficult access of the electrolyte to the whole porous volume) [55], (ii) the occurrence of the ORR through two consecutive catalytic steps [56], and/or (iii) the presence of a second set of active sites with distant onset potentials and slow kinetics. Moreover, the absence of a clear mass transport limited current plateau at low potential (i.e., below −0.7 V vs. Ag/AgCl) suggests slow kinetics. While the shape of these polarization curves is still opened to debate, LSV curves with similar shapes were reported for TiO₂ and defective TiO_{2-x} single crystals in the ORR in 0.1 M KOH [17]. Besides these considerations, significant differences were observed between the samples prepared herein. Both the onset potential (determined at the base of the first catalytic wave), the half-wave potential ($E_{\text{cat}/2}$, determined at the half of the first catalytic current wave) and the catalytic current (determined at the first plateau region) increased from stoichiometric TiO₂ (i.e., xer-TiO₂ and TiO₂-5-5) to sub-stoichiometric Ti_{*n*}O_{2*n*-1} phases-containing samples (i.e., TiO₂/C-9-1 and TiO₂/C-9-8). Interestingly, TiO₂/C-8-4, free of Ti-suboxide phase, depicts intermediary properties (Figure 7b, Table 2), which can be attributed to the presence of the amorphous carbon coating surrounding the (stoichiometric) TiO₂ nanocrystals. As reported by Pei et al. [17] with TiO₂/C nanocomposites, such enhanced ORR activity may be attributed to a superior electronic conductivity and an improved charge transfer across the TiO₂-carbon interface.

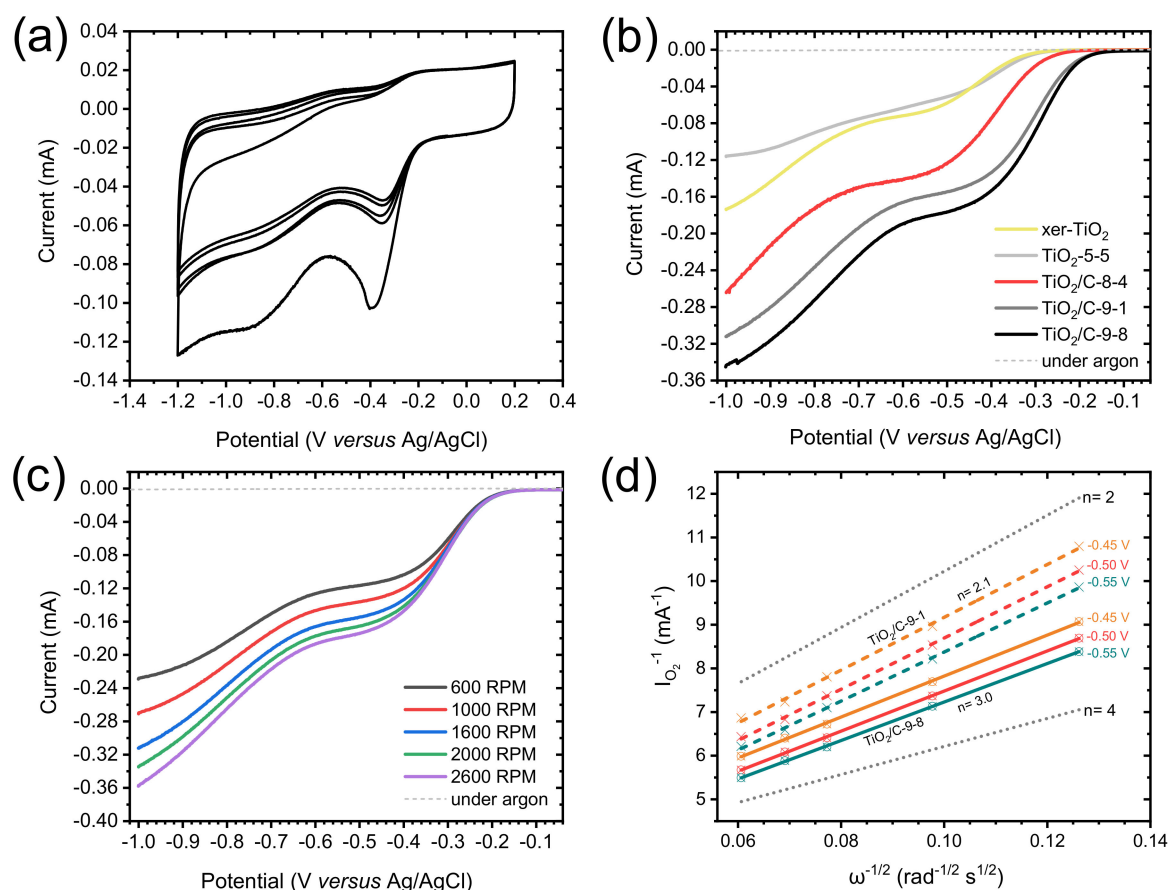


Figure 7. (a) Cyclic voltammogram measured for $\text{TiO}_2/\text{C}-9-1$ in O_2 -saturated 0.1 M KOH solution at a scan rate of 100 mV s^{-1} . (b) Polarization curves measured in O_2 -saturated 0.1 M KOH solution, at a scan rate of 10 mV s^{-1} , and a rotation rate of 1600 rpm for xer-TiO_2 , TiO_2-5-5 and the $\text{TiO}_2/\text{C}-x-y$ series. (c) Polarization curves measured in O_2 -saturated 0.1 M KOH solution (solid lines) for $\text{TiO}_2/\text{C}-9-1$ at different rotation rates from 600 to 2600 rpm , at a scan rate of 10 mV s^{-1} . The dashed lines are the polarization curves measured in Ar -saturated 0.1 M KOH solution, at a scan rate of 10 mV s^{-1} and a rotation rate of 1600 rpm . (d) Koutecky–Levich plots obtained for $\text{TiO}_2/\text{C}-9-1$ (colored dashed lines) and $\text{TiO}_2/\text{C}-9-8$ (colored solid lines) at different voltages (from -0.45 to $-0.55 \text{ V vs. Ag/AgCl}$). The dotted lines correspond to the ideal two electrons process ($n = 2$) and four electrons process ($n = 4$).

Table 2. Electrochemical properties towards the ORR in 0.1 M KOH of xer-TiO_2 , TiO_2-5-5 and the different $\text{TiO}_2/\text{C}-x-y$ samples studied herein. Comparison with a commercial Pt/C , $20 \text{ wt.}\%$, catalyst.

Sample	Onset potential (V) ^a	$E_{\text{cat}/2}$ (V) ^b	I_{cat} (mA mg^{-1}) ^c	I_{k} (mA mg^{-1}) ^d	$n_{\text{electrons}}$ ^e
xer-TiO_2	-0.20	-0.43	1.27	n/a	n/a
TiO_2-5-5	-0.20	-0.40	1.44	n/a	n/a
$\text{TiO}_2/\text{C}-8-4$	-0.16	-0.39	2.80	n/a	n/a
$\text{TiO}_2/\text{C}-9-1$	-0.09	-0.31	3.32	5.1	2.1 ± 0.2
$\text{TiO}_2/\text{C}-9-8$	-0.09	-0.30	3.78	5.3	3.0 ± 0.2
Pt/C , $20 \text{ wt.}\%$	-0.01	-0.13	4.80	10.0	3.8 ± 0.1

^a Onset potential determined at the base of the catalytic wave. ^b $E_{\text{cat}/2}$ is the potential determined at half of the catalytic current according to Appel et al. [57]. ^c I_{cat} is the catalytic current determined at the first plateau region in the potential range from -0.4 to -0.7 V . ^d Kinetic current extracted from Koutecky–Levich (KL) plots at $-0.4 \text{ V vs. Ag/AgCl}$. ^e Average electron transfer number extracted from KL plots applied from -0.35 to $-0.55 \text{ V vs. Ag/AgCl}$.

To further investigate the electrocatalytic mechanisms involved herein, polarization curves were acquired at different rotation rates, from 600 to 2600 rpm (Figure 7c). The reciprocal current ($I_{\text{O}_2}^{-1}$) was

plotted against the reciprocal root of the angular rotation rate ($\omega^{-1/2}$) at various potentials from -0.3 to -0.55 V vs. Ag/AgCl, giving Koutecky–Levich (KL) plots (Figure 7d and Appendix A). These plots were drawn for TiO₂/C-9-1 and TiO₂/C-9-8. While the slope gives information about the electron transfer number, the y-intercept (equal to the reciprocal kinetic current) gives information about the kinetic current and the rate constant of the reaction [44]. As for kinetic currents, they are similar for TiO₂/C-9-1 and TiO₂/C-9-8, but lower than Pt/C, 20 wt.%, used as a benchmark (Table 2 and Appendix B, Figure A1). This result supports low rate constants for TiO₂/C-9-1 and TiO₂/C-9-8 as compared with Pt/C, 20 wt.%. As for electron transfer numbers, KL plots revealed a clear difference between the two Ti_nO_{2n-1}@TiO₂/C nanocomposites. While TiO₂/C-9-1 seems to be very selective for the two electrons process, TiO₂/C-9-8 depicts an intermediary behavior between the two electrons process and the four electrons process (Figure 7d). While not fully understood, this difference may be attributed to enhanced electronic conductivity and charge transfer across the TiO₂-carbon interface, due to the longer plateau duration at 950 °C during carbothermal reduction.

4. Discussion and Conclusions

Overall, the NHSG route allowed producing Ti_nO_{2n-1}@TiO₂/C nanocomposites by a straightforward solvent-free, additive-free approach that meets the challenge of atom economy, as it merely involves TiCl₄ and THF in stoichiometric amounts. Despite a theoretically sufficient C:Ti molar ratio, the carbothermal reduction, even after long treatment, was incomplete as compared with recent studies reported in literature [28,29,32]. NHSG routes usually yield highly condensed and well crystallized metal oxide particles [33], which is also true in the present case. Thus, one may assume that these native TiO₂ anatase nanocrystals are more resistant to the carbothermal reduction, which was most probably limited here to the titanium atoms located at the very surface of the nanoparticles or to the smallest nanocrystals. Besides, the nature and the reactivity of the carbon produced by the NHSG route may also be a source of explanation of the incomplete carbothermal reduction, since it has been reported that the type of carbon plays an important role on the reducibility of TiO₂ [58].

Anyway, the NHSG route seems promising and should be further explored. To better understand the mechanisms involved in the carbothermal reduction and to identify the key parameters, other NHSG routes, with various oxygen donors and carbon sources, should be considered to yield smaller nanocrystals and/or higher carbon contents. The use of innocuous alternatives to THF, such as polysaccharides [59], should be also investigated to make the whole procedure safer and more sustainable. Besides, alternative reduction protocols are currently considered to yield more advanced reduction reactions, such as higher temperatures, the use of hydrogen gas or the addition of oxygen scavengers. To conclude, we believe that these preliminary results will open a window of opportunity for the design of metal suboxides/carbon nanocomposites through atom-economic NHSG routes. This approach should not be limited to titanium suboxides and can easily be extended to other metal oxides.

Author Contributions: Conceptualization, N.B.; validation, R.B., P.H.M., and N.B.; investigation, S.Z.; writing—original draft preparation, N.B.; writing—review and editing, R.B., B.B., and P.H.M.; supervision, R.B. and N.B.; funding acquisition, P.H.M. and R.B. All authors have read and agreed to the published version of the manuscript.

Funding: This research was partially funded by the European Commission in the framework of POROUS4APP project (H2020 GA no. 666157).

Acknowledgments: Nicolas Brun is grateful to Angel Manuel Escamilla-Pérez for fruitful discussions. The authors would like to thank Franck Godiard for TEM and Erwan Oliviero for STEM-EDX.

Conflicts of Interest: The authors declare no conflict of interest.

Appendix A

Koutecky–Levich equation applied herein [44]:

$$\frac{1}{I} = \frac{1}{B} \times \omega^{-\frac{1}{2}} + \frac{1}{I_k} \quad (\text{A1})$$

$$i_{th} B = 0.62 \times n \times F \times A \times \nu^{-\frac{1}{6}} \times C_{O_2} \times D_{O_2}^{\frac{3}{2}} \quad (\text{A2})$$

where, I is the measured catalytic current; I_k is the kinetic current; n is the electron transfer number in half reaction; F is the Faraday constant, i.e., $96\,485.34 \text{ C mol}^{-1}$; A is the electrode surface area in cm^2 (electrode diameter of 0.3 cm); ν is the kinematic viscosity of the electrolyte, i.e., $0.01 \text{ cm}^2 \text{ s}^{-1}$ for KOH at 0.1 M; C_{O_2} is the solubility of O_2 in the electrolyte, i.e., $1.2 \times 10^{-6} \text{ mol cm}^{-3}$ in KOH 0.1 M; D_{O_2} is the diffusion coefficient of O_2 in the electrolyte, i.e., $1.9 \times 10^{-5} \text{ cm}^2 \text{ s}^{-1}$ in KOH 0.1 M at $25 \text{ }^\circ\text{C}$; and ω is the angular rotation rate in rad s^{-1} .

Appendix B

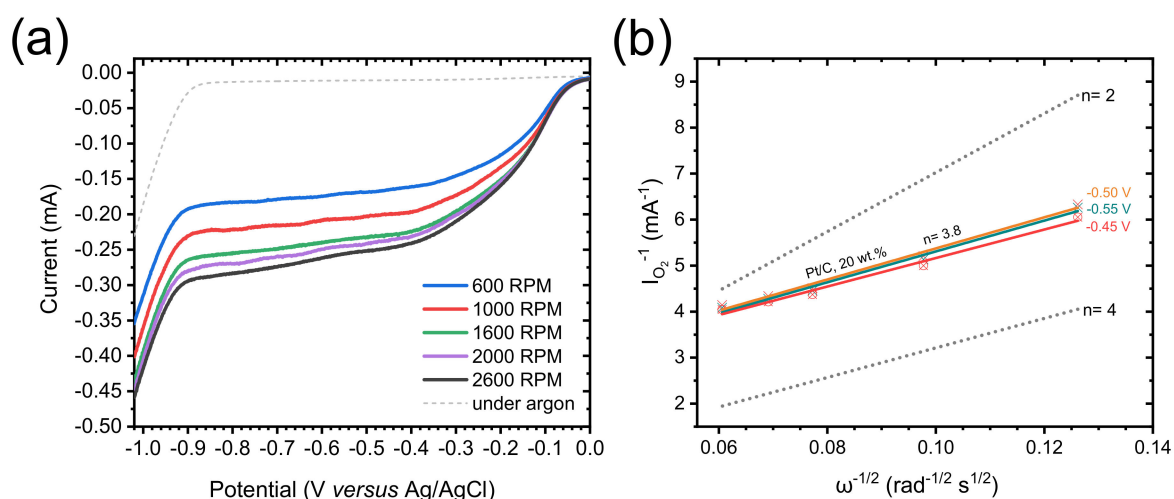


Figure A1. (a) Polarization curves measured in O_2 -saturated 0.1 M KOH solution (solid lines) for Pt/C, 20 wt.%, at different rotation rates from 600 to 2600 rpm, at a scan rate of 10 mV s^{-1} . The dashed line is the polarization curve measured in argon-saturated 0.1 M KOH solution, at a scan rate of 10 mV s^{-1} and a rotation rate of 1600 rpm. (b) Koutecky–Levich plots obtained for Pt/C, 20 wt.% (colored solid lines), at different voltages (from -0.45 to $-0.55 \text{ V vs. Ag/AgCl}$). The dotted lines correspond to the ideal two electrons process ($n = 2$) and four electrons process ($n = 4$).

References

- Harada, S.; Tanaka, K.; Inui, H. Thermoelectric properties and crystallographic shear structures in titanium oxides of the Magneli phases. *J. Appl. Phys.* **2010**, *108*, 083703. [\[CrossRef\]](#)
- Padilha, A.C.M.; Osorio-Guillen, J.M.; Rocha, A.R.; Dalpian, G.M. Ti_nO_{2n-1} Magneli phases studied using density functional theory. *Phys. Rev. B* **2014**, *90*, 035213. [\[CrossRef\]](#)
- Padilha, A.C.M.; Raebiger, H.; Rocha, A.R.; Dalpian, G.M. Charge storage in oxygen deficient phases of TiO_2 : Defect Physics without defects. *Sci. Rep.* **2016**, *6*, 28871. [\[CrossRef\]](#) [\[PubMed\]](#)
- Szot, K.; Rogala, M.; Speier, W.; Klusek, Z.; Besmehn, A.; Waser, R. TiO_2 -a prototypical memristive material. *Nanotechnology* **2011**, *22*, 254001. [\[CrossRef\]](#)
- Anderson, J.S.; Tilley, R.J.D. Crystallographic Shear in Oxygen-Deficient Rutile: An Electron Microscope Study. *J. Solid State Chem.* **1970**, *2*, 472–482. [\[CrossRef\]](#)
- Chen, X.B.; Liu, L.; Huang, F.Q. Black titanium dioxide (TiO_2) nanomaterials. *Chem. Soc. Rev.* **2015**, *44*, 1861–1885. [\[CrossRef\]](#)

7. Cho, E.; Han, S.; Ahn, H.S.; Lee, K.R.; Kim, S.K.; Hwang, C.S. First-principles study of point defects in rutile TiO_{2-x} . *Phys. Rev. B* **2006**, *73*, 193202. [[CrossRef](#)]
8. Andersson, S.; Collen, B.; Kuylenstierna, U.; Magneli, A. Phase Analysis Studies on the Titanium-Oxygen System. *Acta Chem. Scand.* **1957**, *11*, 1641–1652. [[CrossRef](#)]
9. Andersson, S.; Collen, B.; Kruuse, G.; Kuylenstierna, U.; Magneli, A.; Pestmalis, H.; Asbrink, S. Identification of Titanium Oxides by X-Ray Powder Patterns. *Acta Chem. Scand.* **1957**, *11*, 1653–1657. [[CrossRef](#)]
10. Asbrink, S.; Magneli, A. Crystal Structure Studies on Trittanium Pentoxide, Ti_3O_5 . *Acta Crystallogr.* **1959**, *12*, 575–581. [[CrossRef](#)]
11. Rajaraman, T.S.; Parikh, S.P.; Gandhi, V.G. Black TiO_2 : A review of its properties and conflicting trends. *Chem. Eng. J.* **2020**, *389*, 123918. [[CrossRef](#)]
12. Bartholomew, R.F.; Frankl, D.R. Electrical Properties of Some Titanium Oxides. *Phys. Rev.* **1969**, *187*, 828–833. [[CrossRef](#)]
13. Han, W.Q.; Zhang, Y. Magneli phases $\text{Ti}_n\text{O}_{2n-1}$ nanowires: Formation, optical, and transport properties. *Appl. Phys. Lett.* **2008**, *92*, 203117. [[CrossRef](#)]
14. Niu, M.; Tan, H.Q.; Cheng, D.J.; Sun, Z.C.; Cao, D.P. Bandgap engineering of Magneli phase $\text{Ti}_n\text{O}_{2n-1}$: Electron-hole self-compensation. *J. Chem. Phys.* **2015**, *143*, 054701. [[CrossRef](#)] [[PubMed](#)]
15. Feng, H.F.; Xu, Z.F.; Ren, L.; Liu, C.; Zhuang, J.C.; Hu, Z.P.; Xu, X.; Chen, J.; Wang, J.O.; Hao, W.C.; et al. Activating Titania for Efficient Electrocatalysis by Vacancy Engineering. *ACS Catal.* **2018**, *8*, 4288–4293. [[CrossRef](#)]
16. Oturan, N.; Ganiyu, S.O.; Raffy, S.; Oturan, M.A. Sub-stoichiometric titanium oxide as a new anode material for electro-Fenton process: Application to electrocatalytic destruction of antibiotic amoxicillin. *Appl. Catal. B-Environ.* **2017**, *217*, 214–223. [[CrossRef](#)]
17. Pei, D.N.; Gong, L.; Zhang, A.Y.; Zhang, X.; Chen, J.J.; Mu, Y.; Yu, H.Q. Defective titanium dioxide single crystals exposed by high-energy {001} facets for efficient oxygen reduction. *Nat. Commun.* **2015**, *6*, 8696. [[CrossRef](#)]
18. Yao, C.H.; Li, F.; Li, X.; Xia, D.G. Fiber-like nanostructured Ti_4O_7 used as durable fuel cell catalyst support in oxygen reduction catalysis. *J. Mater. Chem.* **2012**, *22*, 16560–16565. [[CrossRef](#)]
19. Massazza, D.; Parra, R.; Busalmen, J.P.; Romeo, H.E. New ceramic electrodes allow reaching the target current density in bioelectrochemical systems. *Energ. Environ. Sci.* **2015**, *8*, 2707–2712. [[CrossRef](#)]
20. Domaschke, M.; Zhou, X.M.; Wergen, L.; Romeis, S.; Miehlich, M.E.; Meyer, K.; Peukert, W.; Schmuki, P. Magneli-Phases in Anatase Strongly Promote Cocatalyst-Free Photocatalytic Hydrogen Evolution. *ACS Catal.* **2019**, *9*, 3627–3632. [[CrossRef](#)]
21. Hamad, H.; Bailon-Garcia, E.; Maldonado-Hodar, F.J.; Perez-Cadenas, A.F.; Carrasco-Marin, F.; Morales-Torres, S. Synthesis of Ti_xO_y nanocrystals in mild synthesis conditions for the degradation of pollutants under solar light. *Appl. Catal. B-Environ.* **2019**, *241*, 385–392. [[CrossRef](#)]
22. An, X.Q.; Hu, C.Z.; Liu, H.J.; Qu, J.H. Oxygen vacancy mediated construction of anatase/brookite heterophase junctions for high-efficiency photocatalytic hydrogen evolution. *J. Mater. Chem. A* **2017**, *5*, 24989–24994. [[CrossRef](#)]
23. Negi, S.S. Enhanced light harvesting and charge separation over wormhole mesoporous TiO_{2-x} nanocrystallites towards efficient hydrogen generation. *Sustain. Energ. Fuels* **2019**, *3*, 1191–1200. [[CrossRef](#)]
24. Tao, X.Y.; Wang, J.G.; Ying, Z.G.; Cai, Q.X.; Zheng, G.Y.; Gan, Y.P.; Huang, H.; Xia, Y.; Liang, C.; Zhang, W.K.; et al. Strong Sulfur Binding with Conducting Magneli-Phase $\text{Ti}_n\text{O}_{2n-1}$ Nanomaterials for Improving Lithium-Sulfur Batteries. *Nano Lett.* **2014**, *14*, 5288–5294. [[CrossRef](#)] [[PubMed](#)]
25. Wei, H.; Rodriguez, E.F.; Best, A.S.; Hollenkamp, A.F.; Chen, D.H.; Caruso, R.A. Chemical Bonding and Physical Trapping of Sulfur in Mesoporous Magneli Ti_4O_7 Microspheres for High- Performance Li-S Battery. *Adv. Energy Mater.* **2017**, *7*, 1601616. [[CrossRef](#)]
26. Kitada, A.; Hasegawa, G.; Kobayashi, Y.; Kanamori, K.; Nakanishi, K.; Kageyama, H. Selective Preparation of Macroporous Monoliths of Conductive Titanium Oxides $\text{Ti}_n\text{O}_{2n-1}$ ($n = 2, 3, 4, 6$). *J. Am. Chem. Soc.* **2012**, *134*, 10894–10898. [[CrossRef](#)]
27. Azor-Lafarga, A.; Ruiz-Gonzalez, L.; Parras, M.; Portehault, D.; Sanchez, C.; Gonzalez-Calbet, J.M. Modified Synthesis Strategies for the Stabilization of low n $\text{Ti}_n\text{O}_{2n-1}$ Magneli Phases. *Chem. Rec.* **2018**, *18*, 1105–1113. [[CrossRef](#)]

28. Portehault, D.; Maneeratana, V.; Candolfi, C.; Deschler, N.; Veremchuk, I.; Grin, Y.; Sanchez, C.; Antonietti, M. Facile General Route toward Tunable Magneli Nanostructures and Their Use As Thermoelectric Metal Oxide/Carbon Nanocomposites. *ACS Nano* **2011**, *5*, 9052–9061. [[CrossRef](#)]
29. Huang, S.S.; Lin, Y.H.; Chuang, W.; Shao, P.S.; Chuang, C.H.; Lee, J.F.; Lu, M.L.; Weng, Y.T.; Wu, N.L. Synthesis of High-Performance Titanium Sub-Oxides for Electrochemical Applications Using Combination of Sol-Gel and Vacuum-Carbothermic Processes. *ACS Sustain. Chem. Eng.* **2018**, *6*, 3162–3168. [[CrossRef](#)]
30. Tominaka, S.; Tsujimoto, Y.; Matsushita, Y.; Yamaura, K. Synthesis of Nanostructured Reduced Titanium Oxide: Crystal Structure Transformation Maintaining Nanomorphology. *Angew. Chem. Int. Edit.* **2011**, *50*, 7418–7421. [[CrossRef](#)]
31. Kitada, A.; Hasegawa, G.; Kobayashi, Y.; Miyazaki, K.; Abe, T.; Kanamori, K.; Nakanishi, K.; Kageyama, H. Hierarchically Porous Monoliths of Oxygen-deficient Anatase TiO_{2-x} with Electronic Conductivity. *RSC Adv.* **2013**, *3*, 26475. [[CrossRef](#)]
32. Mei, S.L.; Jafta, C.J.; Lauermann, I.; Ran, Q.; Kargell, M.; Ballauff, M.; Lu, Y. Porous Ti₄O₇ Particles with Interconnected-Pore Structure as a High-Efficiency Polysulfide Mediator for Lithium-Sulfur Batteries. *Adv. Funct. Mater.* **2017**, *27*, 1701176. [[CrossRef](#)]
33. Mutin, P.H.; Vioux, A. Recent advances in the synthesis of inorganic materials via non-hydrolytic condensation and related low-temperature routes. *J. Mater. Chem. A* **2013**, *1*, 11504–11512. [[CrossRef](#)]
34. Niederberger, M.; Garnweitner, G. Organic reaction pathways in the nonaqueous synthesis of metal oxide nanoparticles. *Chem. Eur. J.* **2006**, *12*, 7282–7302. [[CrossRef](#)] [[PubMed](#)]
35. Debecker, D.P.; Hulea, V.; Mutin, P.H. Mesoporous mixed oxide catalysts via non-hydrolytic sol-gel: A review. *Appl. Catal. A Gen.* **2013**, *451*, 192–206. [[CrossRef](#)]
36. Pinna, N.; Niederberger, M. Surfactant-free nonaqueous synthesis of metal oxide nanostructures. *Angew. Chem. Int. Edit.* **2008**, *47*, 5292–5304. [[CrossRef](#)]
37. Deshmukh, R.; Niederberger, M. Mechanistic Aspects in the Formation, Growth and Surface Functionalization of Metal Oxide Nanoparticles in Organic Solvents. *Chem. Eur. J.* **2017**, *23*, 8542–8570. [[CrossRef](#)] [[PubMed](#)]
38. Niederberger, M.; Garnweitner, G.; Pinna, N.; Neri, G. Non-aqueous routes to crystalline metal oxide nanoparticles: Formation mechanisms and applications. *Prog. Solid State Chem.* **2005**, *33*, 59–70. [[CrossRef](#)]
39. Niederberger, M. Nonaqueous sol-gel routes to metal oxide nanoparticles. *Acc. Chem. Res.* **2007**, *40*, 793–800. [[CrossRef](#)]
40. Hay, J.N.; Raval, H.M. Synthesis of organic-inorganic hybrids via the non-hydrolytic sol-gel process. *Chem. Mater.* **2001**, *13*, 3396–3403. [[CrossRef](#)]
41. Wang, Y.H.; Alauzun, J.G.; Mutin, P.H. Water-Stable, Nonsiliceous Hybrid Materials with Tunable Porosity and Functionality: Bridged Titania-Bisphosphonates. *Chem. Mater.* **2020**, *32*, 2910–2918. [[CrossRef](#)]
42. Escamilla-Perez, A.M.; Louvain, N.; Boury, B.; Brun, N.; Mutin, P.H. Ethers as Oxygen Donor and Carbon Source in Non-hydrolytic Sol-Gel: One-Pot, Atom-Economic Synthesis of Mesoporous TiO₂-Carbon Nanocomposites. *Chem. Eur. J.* **2018**, *24*, 4982–4990. [[CrossRef](#)] [[PubMed](#)]
43. Han, X.Y.; Russo, P.A.; Goubard-Bretesche, N.; Patane, S.; Santangelo, S.; Zhang, R.; Pinna, N. Exploiting the Condensation Reactions of Acetophenone to Engineer Carbon-Encapsulated Nb₂O₅ Nanocrystals for High-Performance Li and Na Energy Storage Systems. *Adv. Energy Mater.* **2019**, *9*, 1902813. [[CrossRef](#)]
44. Masa, J.; Batchelor-McAuley, C.; Schuhmann, W.; Compton, R.G. Koutecky-Levich analysis applied to nanoparticle modified rotating disk electrodes: Electrocatalysis or misinterpretation? *Nano Res.* **2014**, *7*, 71–78. [[CrossRef](#)]
45. Escamilla-Perez, A.M.; Louvain, N.; Kaschowitz, M.; Freunberger, S.; Fontaine, O.; Boury, B.; Brun, N.; Mutin, P.H. Lithium insertion properties of mesoporous nanocrystalline TiO₂ and TiO₂-V₂O₅ microspheres prepared by non-hydrolytic sol-gel. *J. Sol-Gel Sci. Technol.* **2016**, *79*, 270–278. [[CrossRef](#)]
46. Nolan, N.T.; Seery, M.K.; Pillai, S.C. Spectroscopic Investigation of the Anatase-to-Rutile Transformation of Sol-Gel-Synthesized TiO₂ Photocatalysts. *J. Phys. Chem. C* **2009**, *113*, 16151–16157. [[CrossRef](#)]
47. Tsumura, T.; Kojitani, N.; Izumi, I.; Iwashita, N.; Toyoda, M.; Inagaki, M. Carbon coating of anatase-type TiO₂ and photoactivity. *J. Mater. Chem.* **2002**, *12*, 1391–1396. [[CrossRef](#)]
48. Escamilla-Pérez, A.M. Non-hydrolytic sol-gel synthesis of TiO₂-based electrode materials for Li-ion batteries. Ph.D. Thesis, University Montpellier, Montpellier, France, September 2018.
49. Thommes, M. Physical Adsorption Characterization of Nanoporous Materials. *Chem. Ing. Tech.* **2010**, *82*, 1059–1073. [[CrossRef](#)]

50. Dai, L.M.; Xue, Y.H.; Qu, L.T.; Choi, H.J.; Baek, J.B. Metal-Free Catalysts for Oxygen Reduction Reaction. *Chem. Rev.* **2015**, *115*, 4823–4892. [[CrossRef](#)]
51. Shao, M.H.; Chang, Q.W.; Dodelet, J.P.; Chenitz, R. Recent Advances in Electrocatalysts for Oxygen Reduction Reaction. *Chem. Rev.* **2016**, *116*, 3594–3657. [[CrossRef](#)]
52. Ge, X.M.; Sumboja, A.; Wu, D.; An, T.; Li, B.; Goh, F.W.T.; Hor, T.S.A.; Zong, Y.; Liu, Z.L. Oxygen Reduction in Alkaline Media: From Mechanisms to Recent Advances of Catalysts. *ACS Catal.* **2015**, *5*, 4643–4667. [[CrossRef](#)]
53. Li, Y.G.; Dai, H.J. Recent advances in zinc-air batteries. *Chem. Soc. Rev.* **2014**, *43*, 5257–5275. [[CrossRef](#)] [[PubMed](#)]
54. Ramaswamy, N.; Mukerjee, S. Alkaline Anion-Exchange Membrane Fuel Cells: Challenges in Electrocatalysis and Interfacial Charge Transfer. *Chem. Rev.* **2019**, *119*, 11945–11979. [[CrossRef](#)] [[PubMed](#)]
55. Brun, N.; Wohlgemuth, S.A.; Osiceanu, P.; Titirici, M.M. Original design of nitrogen-doped carbon aerogels from sustainable precursors: Application as metal-free oxygen reduction catalysts. *Green Chem.* **2013**, *15*, 2514–2524. [[CrossRef](#)]
56. Pham-Truong, T.N.; Petenzi, T.; Ranjan, C.; Randriamahazaka, H.; Ghilane, J. Microwave assisted synthesis of carbon dots in ionic liquid as metal free catalyst for highly selective production of hydrogen peroxide. *Carbon* **2018**, *130*, 544–552. [[CrossRef](#)]
57. Appel, A.M.; Helm, M.L. Determining the Overpotential for a Molecular Electrocatalyst. *ACS Catal.* **2014**, *4*, 630–633. [[CrossRef](#)]
58. Jha, A.; Yoon, S.J. Formation of titanium carbonitride phases via the reduction of TiO₂ with carbon in the presence of nitrogen. *J. Mater. Sci.* **1999**, *34*, 307–322. [[CrossRef](#)]
59. Kim, S.; De Bruyn, M.; Alauzun, J.G.; Louvain, N.; Brun, N.; Macquarrie, D.J.; Stievano, L.; Mutin, P.H.; Monconduit, L.; Boury, B. Dehydration of Alginate Cryogel by TiCl₄ vapor: Direct Access to Mesoporous TiO₂@C Nanocomposites and Their Performance in Lithium-Ion Batteries. *ChemSuschem* **2019**, *12*, 2660–2670. [[CrossRef](#)]



© 2020 by the authors. Licensee MDPI, Basel, Switzerland. This article is an open access article distributed under the terms and conditions of the Creative Commons Attribution (CC BY) license (<http://creativecommons.org/licenses/by/4.0/>).